Measurement of Transient Blade Passage Loads of a Coaxial Counter-Rotating Rotor in Hover

Daiju Uehara [*] **Jayant Sirohi** [†]
Department of Aerospace Engineering and Engineering Mechanics
The University of Texas at Austin, TX, USA

Roland Feil [‡] **Jürgen Rauleder** [§]
Institute of Helicopter Technology
Technical University of Munich, Germany

This study describes the measurement of transient hub loads and blade deformations due to blade passage in a 1×1-bladed, 2m-diameter rigid coaxial counter-rotating rotor system in hover. The experimental results were analyzed and evaluated in combination with a comprehensive analysis model using CAMRAD II. Lower rotor blade deformations were measured using a time-resolved digital image correlation technique. Rotating modal parameters including natural frequencies and mode shapes were identified from measured time histories of rotor blade deformations using the Complexity Pursuit algorithm. Experimentally identified modal characteristics correlated well with numerical results for the first three modes. The numerical model also predicted the vibratory hub and pitch link loads as well as out-of-plane deformations satisfactorily well and within the measurement uncertainties. The 2/rev blade tip displacement due to blade passage was found to be 6% of the mean tip displacement, and the transient blade motion of the lower rotor blade was found to be larger than that of the upper rotor blade. Additional numerical studies on the aerodynamic angles of attack, the inflow velocities from rotor–rotor interaction, and sectional lift distributions over the upper and lower coaxial rotor disks provided further insight into the sources of transient loads due to blade passage. For example, it was found that the angle of attack on the lower rotor induced by the upper rotor had a maximum at 15° azimuth before the blade passage.

NOMENCLATURE

A	Mixing matrix
C	Damping matrix
C_T	Rotor thrust coefficient, $T/\rho A(\Omega R)^2$
c	chord length, m
F	Force vector
F_{PL}	Pitch link force (positive in tension), N
F_Z	Blade sectional loads (positive upwards), N/m
G	Temporal predictability
i	Index of physical channels
K	Stiffness matrix
M	Mass matrix
N	The number of sample
N_b	Number of blades
n	Noise vector
R	Radius, m
r_{rc}	Root cut-out, m
s	Source vector
T	Rotor thrust (positive upwards), N
t	Time
V_{tip}	Blade tip speed, m/s
v_{int}	interactional inflow velocity, m/s
W	Eigenvectors matrix
$x, \dot{x}, \ddot{x}$	Displacement, velocity, and acceleration vectors
y	Measured response vector
$\bar{y}$	Long-term predictor
$\hat{y}$	Short-term predictor
z_R	Inter-rotor spacing, m
β_p	Pre-cone angle, deg
η	Modal coordinates
σ	Rotor solidity
Φ	Modal matrix
ψ_b	blade azimuth angle, deg
Ω	rotor rotational speed, rpm

[*] Graduate Research Assistant. udaiju9@utexas.edu
[†] Associate Professor. jayant.sirohi@mail.utexas.edu
[‡] Graduate Research Assistant. roland.feil@tum.de
[§] Lecturer. juergen.rauleder@tum.de

Presented at the 44th European Rotorcraft Forum, Delft, The Netherlands, September 18–21, 2018.

Superscripts

L	Lower rotor in coaxial configuration
n	n/rev harmonics component
U	Upper rotor in coaxial configuration

1. INTRODUCTION

Recently, there has been a resurgence of interest in the compound helicopter configuration with a coaxial, counter-rotating (CCR) rotor system. The main advantage of the CCR rotor system compared to a conventional single main rotor is the increased aerodynamic efficiency, or lift-to-equivalent-drag ratio (L/D_e), particularly in high-speed forward flight [1]. The increased L/D_e has been proven during flight testing the X2 Technology^{TM} Demonstrator, a compound helicopter that incorporates a CCR rotor [2], and also by conducted wind tunnel tests of a reduced-scale model CCR rotor [3]. High-speed forward flight relies on a low drag rotor system, which can be achieved in the CCR rotor by closely-spaced rotors, rigid rotor hubs, and stiff rotor blades that carry a lift offset [4].

However, such a rigid lift-offset CCR rotor experiences increased vibrations compared to a conventional articulated single rotor, mainly due to the very high flap bending stiffness necessary to maintain sufficient rotor blade clearance. For example, the vibratory thrust of the lower CCR rotor can be about 11% of the mean thrust in hover [5], and up to 100% in fast forward flight [6]. The vibratory loads were in part exacerbated by the transient aerodynamic loading introduced by the passage of the closely-spaced upper and lower rotor blades. It is thus important to understand the fundamental aerodynamic phenomena responsible for the transient loading, so that the rotor design can be optimized to minimize these vibratory loads. To this end, a key step is to measure and identify the transient aerodynamic forcing due to blade passage.

Typically, fixed-frame or rotating-frame load cells measure a combination of inertial forces and aerodynamic forces. Aerodynamic forces can be estimated from chordwise and spanwise integration of blade surface pressure measurements [7, 8]. Challenges to this approach include structural integration of the pressure transducers, in-situ dynamic calibrations, inertial loading compensation, signal routing and slip-ring capacity, as well as transducer cost. Inertial forces can be estimated from blade deformation measurements. These are typically performed using strain gauges that pose similar challenges as the blade surface pressure transducers, or by non-contact optical methods.

This paper introduces a combined experimental–numerical approach for investigation of transient loads due to blade passage in a CCR rotor system in hover. Experiments were performed on a reduced-scale, 2m-diameter, 1×1-bladed CCR rotor system in hover. The blade deformation over the entire rotor disk was measured using a non-contact optical technique called time-resolved Digital Image Correlation (DIC). A strong point of this methodology is that minimal preparation of the test article is required, i.e., painting the blade surface with a random speckle pattern. In previous work, the DIC methodology was used in conjunction with two high-speed cameras for measuring the blade deformation of an 18-inch-diameter rotor [9, 10]. In this current work, the methodology was extended to the larger test article by incorporating a third high-speed camera; a schematic of the experimental setup is shown in Fig. 1.

The measured blade deformation was used to extract rotating-frame blade natural frequencies and mode shapes using an output-only analysis called Complexity Pursuit. In contrast to classical modal analysis that requires measurement of both the input excitation to a structure and its response, this method only requires measurement of the response of a structure under ambient or operational excitation. In previous work, the authors [9, 10] used this approach to identify the natural frequencies and mode shapes of a 0.4m-diameter rotor. In the current work, the estimated modal properties of the blade and the measured blade deformation for a 2m-diameter, 1×1-bladed CCR rotor system in hover were used to further validate a comprehensive numerical model of the rotor system using CAMRAD II. This model was also used in previous work [11] to predict the unsteady loads and blade deformations for an isolated single rotor. In this current work, the validated analysis was used to further explore the rotor–rotor aerodynamic interactions and unsteady aerodynamic loads responsible for transient blade deflections that were induced by blade passage in the 1×1-bladed CCR rotor.

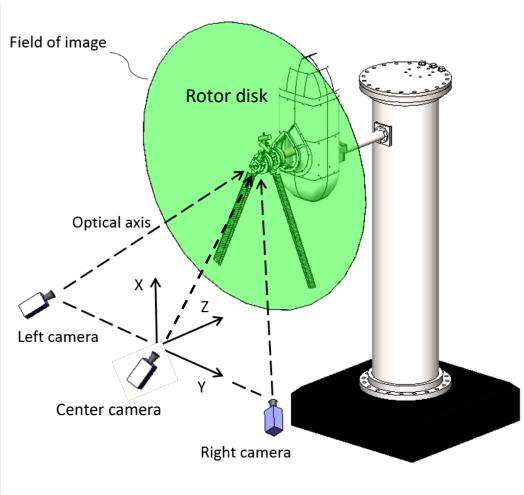

Fig. 1: Schematic of the measurement setup.

2. DESCRIPTION OF EXPERIMENTS

In the present study, it is important to capture images of the rotor blade over the entire rotor disk so that a continuous time series of rotor blade deformation can be generated and analyzed. To this end, the rotor shaft axis is aligned horizontally to allow optical access to the entire rotor disk, as shown in Fig. 1. For simplicity, the CCR rotor was configured in such a way that a single rotor blade was attached to each rotor and the blade passage occurred twice over one revolution at 0° and 180° of blade azimuth, with zero blade azimuth pointing downwards.

Drive System and Fixed Frame Instrumentation

A hydraulic power unit provides rotor power through a transmission drive with synchronous 64-toothed belts and pulleys. A serpentine belt with an idler enables the upper and lower rotor to spin in opposite directions at the same rotational speed. The test stand can be configured for a coaxial counter-rotating rotor or a single isolated rotor. Fixed frame instrumentation includes a two-axis accelerometer to measure the vibration of the test stand, four bearing temperature sensors, and a 4096-per-revolution incremental encoder mounted on the motor drive shaft for rotational speed measurement. The horizontally-oriented coaxial rotor stand is shown in Fig. 2.

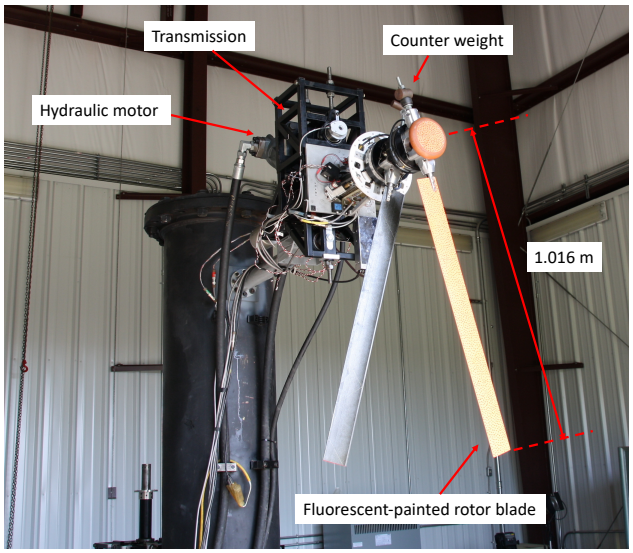

Fig. 2: The horizontally-oriented 1×1-bladed coaxial rotor stand.

Rotor Configuration

Each rotor consists of a single rotor blade and counterweight attached to a hingeless hub that is stiff in flap and lead-lag, and with a bearing for blade pitch. The rotor blade is untwisted with constant chord and a uniform VR-12 airfoil including a 5% trailing edge tab. The blade was fabricated with a foam core and wrapped with carbon fiber prepreg skin. Tungsten masses are located along the leading edge of the blade to adjust the chordwise center of mass. Collective and cyclic pitch of each rotor are controlled by two independent swashplates, each actuated by three linear servos. The rotor system is trimmed by adjusting the collectives of each rotor so that the total yaw moment of the system becomes zero.

Upper and lower rotor hub loads were measured using two 6-component load cells (ATI Omega-160) installed below each rotor hub in the rotating frame. The resolution of forces and moments were 0.75 N and 0.025 Nm respectively. Bias uncertainties of side forces, vertical (axial) force, and three moments were ± 4 N, ± 8 N, and ± 0.5 Nm, respectively. Rotating pitch link loads were measured by axial compression-tension load cells attached to each pushrod, with a full scale range of ± 250 N and a resolution of ± 0.5 N. The measured pitch link loads in the rotating frame represent the variation of control forces of each rotor as a function of blade azimuth. Due to the geometry of the experimental assembly, these control forces were added to the measured hub loads to obtain rotating-frame rotor loads.

Blade Deformation Measurement

The blade deformation measurements were performed by means of the DIC technique. The present study used stereoscopic DIC with three high-speed cameras to obtain full three-dimensional displacement fields on the rotor blade; the camera setup is shown in Fig. 3. The first and second cameras (Phantom Miro M310 with Nikon NIKKOR f/1.8D 35 mm lenses) were mounted so that each camera captured the entire rotor disk and the third camera (Phantom Miro M310 with a zoom lens) was mounted on a tripod located between the first and the second camera. At some azimuthal locations, images taken by the left and right cameras (Camera No. 1 and Camera No. 2) were distorted due to large parallax; these images were corrected using images taken by the middle camera (Camera No. 3).

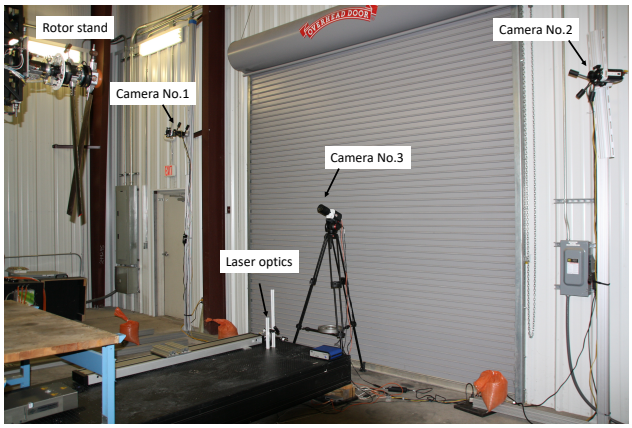

Fig. 3: DIC measurement setup.

Fluorescent orange paint was applied on the bottom surface of the lower rotor blade and stochastic black dots (artificial speckle pattern) were painted on the surface. A Nd:YLF pulsed laser strobe with a wavelength of 527 nm was used to illuminate the entire rotor disk at any desired instant of time; low pass filters on the camera lenses allowed only the light flouresced from the blade surface to be captured by the cameras. The incremental encoder on the drive shaft was used to generate a 32-per-revolution pulse train, which triggers laser strobing and image acquisition at 32 evenly-spaced azimuthal locations. Undeformed reference images were first taken by rotating the rotor at very low angular velocity (approximately 60 RPM). Then, images were captured by the three high-speed cameras when the rotor system was operated at target rotational speed and thrust level. Figure 4 shows the actual images taken by three cameras triggered at a certain azimuthal angle. Note that the DIC deformation measurement was performed only on the lower rotor blade of the coaxial system.

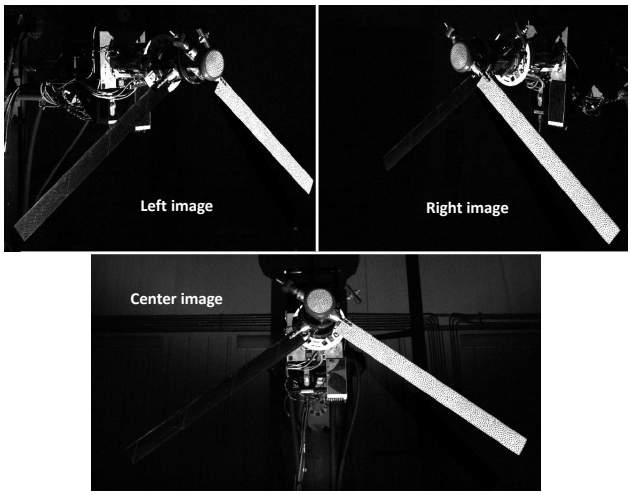

Fig. 4: Digital images taken by three high-speed cameras.

To recover the three-dimensional deformation field, each image was divided into a number of interrogation windows. Corresponding interrogation windows in two different camera images were found by a correlation process that identified the same speckle pattern inside both windows. A displacement vector was generated for each interrogation window. An important step for obtaining three-dimensional displacements from the images is the calibration of the high-speed camera system. Figure 5 shows the calibration process for the high-speed cameras, using a standard calibration target plate placed at the rotor plane. Knowledge of the size and location of the target plate with respect to the rotor plane, enables calculation of a mapping function between global coordinates and camera image plane coordinates. Three-dimensional deformation of the rotor blade was calculated at a total of 2020 (20 chordwise and 101 spanwise) locations. All image processing was performed by a commercial DIC software (LaVision DaVis 8). The accuracy of the vectors depends on the size of the interrogation window (21 $\times$ 21 pixels in this case); according to the software manual, the displacement accuracy was estimated to be 0.01%R (0.1 mm), while the spatial resolution of the displacement field was estimated to be 0.2%R (2 mm).

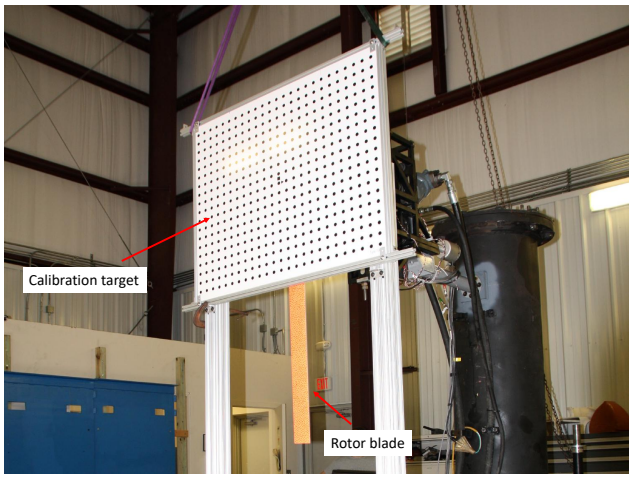

Fig. 5: Camera calibration setup.

Test Envelope

Experiments were performed at several different operating conditions. First, the 1$\times$1-bladed CCR rotor was tested at a collective pitch angle of 0° and at -2°. At these low collective pitch angles, the wake was in close proximity to the rotor blades creating an unsteady random excitation that was observed and captured by the three high-speed cameras. These data were used to extract the rotating natural frequencies of the lower rotor blade. Then, the CCR rotor was tested at high thrust, where the lower rotor produced approximately 80 N of rotor thrust, corresponding to blade loadings (C_T/σ), of about 0.09. The CCR rotor was spun at 900 RPM and was trimmed to a balanced torque condition, i.e., equal and opposite torque on the upper and lower rotors. At all the test conditions, hub and pitch link loads as well as the lower rotor blade deformation were measured simultaneously, synchronized by the optical encoder; data was recorded for 300 revolutions at each test condition.

3. MODELING APPROACH

A comprehensive analysis of the presented 1$\times$1-bladed rotor configuration was performed using CAMRAD II [12]. The rotor parameters, blade structural properties, and operating conditions of the CAMRAD II model were identical to those of the experimental setup (see Table 1), although the counterweights mounted to the rotor shafts of upper and lower rotor were not modeled. For validation of the analytical model, measurements obtained with the previously described experimental setup were used. In previous work,

this model was validated [1,6,13] for the 2×2-bladed CCR rotor system (all other specifications of the rotor system being identical to the 1×1-bladed coaxial rotor setup). Comparisons to the experiment and validation including blade dynamics and transient blade deformations with the 1×1 CCR rotor system were also performed [11] and extended in the current work with a new set of analytical correlations and experiments including new measurement techniques.

Table 1: Rotor parameters.

Parameter	Single	Coaxial
N_b	1	1×1
R, m	1.016	1.016
r_{rc}, m	0.122	0.122
z_R, m	-	0.140 m (13.8 %R)
Airfoil section	VR-12	VR-12
β_p, deg	3	3
c, m	0.080	0.080
σ	0.025	0.05 (total)
V_{tip}, m/s	95.8	95.8
Ω, RPM	900	900

CAMRAD II is an aeromechanics analysis for rotorcraft that incorporates a combination of advanced treatments of rotating systems, including multibody dynamics, nonlinear finite element methods, and rotor blade and wake aerodynamics models of various fidelity levels, also differing significantly in the associated computational expense. In this current study, the rotor blade aerodynamics were modeled based on lifting line theory using steady two-dimensional airfoil characteristics. These airfoil characteristics of the VR-12 airfoil section were obtained from CFD computations for multiple Mach numbers and showed good correlation to experiments [14].

The aerodynamics model consisted of 22 aerodynamic panels and with nine structural beam elements per blade. Unless otherwise noted, 24 azimuthal positions were calculated per rotor revolution. A computationally efficient free vortex wake (FVW) method was used to compute the rotor wake and aerodynamic interactions between the wakes of the two rotors inducing transient loads. FVW methods discretize the rotor wake into vortex filaments and then calculate the velocities induced by the filaments on each other and on the flow field using the Biot–Savart law [15, 16]. In the current FVW analysis, a multiple-trailer model with two trailers and vortex roll-up was used that previously showed good predictions of the lift distribution, vibrations, and tip vortex wake geometry [17]. Bagai–Leishman's vorticity distribution [18], a Bagai–Leishman vortex core radius growth model [15] and a general free wake geometry allowed for aerodynamic rotor–rotor interactions to be accounted for. The near wake was truncated after 60 degrees of wake age. To sufficiently account for blade–vortex or vortex–vortex interactions that may affect the results, the far wake was computed for ten rotor revolutions before it was truncated, with the wake distortion being extended by another five rotor revolutions.

Table 2: Homogeneous blade inertial and elastic properties.

Property	Value
Blade mass	162 g
Blade section mass	0.18 kg/m
Flap bending stiffness	22 Nm^2
Lag bending stiffness	800 Nm^2
Torsional stiffness	23 Nm^2
Axial stiffness	9280000 N

For the current aeromechanics model, the rectangular and untwisted composite blades of the rotor had homogeneous inertial and elastic properties according to the measured values listed in Table 2. These blade elastic properties were obtained from static blade bending tests. Blade inboard sectional parameters were adjusted to match the non-rotating natural frequencies with the measured data. This is a reasonable and physics-based assumption because, for mounting purposes, the blade had three holes at the inboard sections, decreasing, e.g., the lag stiffness, accordingly. Table 3 shows the control system's main properties, including pitch horn length, pitch link stiffnesses, and swashplate locations. Because of the finite stiffness of the control system, in the modeling approach, elastic pitch links were used to account for the combined elasticities within the entire control system. Resulting rotating natural frequencies were computed and validated against rotating measurements that are shown later.

In case of the 1×1-bladed CCR rotor system, a two-degree-of-freedom trim was used. The two residuals for the coaxial trim algorithm were the lower rotor disk loading and rotor system torque balance. These were set as input to the trim routine. Upper and lower rotor collectives (i.e., the two trim variables) were then adjusted by the trim algorithm according to the rotor operating condition. This trim algorithm provided the capability to individually target a particular lower coaxial rotor thrust, and it is the same control strategy as used on the model rotor test setup. Trim convergence criteria was set to less than 0.1%.

Table 3: Control system parameters.

Parameter	Upper Rotor	Lower Rotor
Pitch horn length	0.013 m	0.0348 m
Pitch link stiffness	7.0×10^5 N/m	7.3×10^5 N/m
Swashplate below hub (Pitch link length)	0.873 m	0.1625 m

4. RESULTS AND DISCUSSION

In this section, the unique characteristics of the coaxial rotor system are comprehensively discussed from several different perspectives. The rotor blade structural characteristics of the coaxial rotor system are first presented with comparison between measured and numerically (CAMRAD II)

predicted results. Measured and predicted transient rotor blade deformations, hub loads, and pitch link loads due to the periodic blade passages are then discussed and correlated. In order to provide further insight into the sources of the transient loads, i.e., the complex aerodynamic interactions between two coaxial rotors, numerical studies are extended to the blade sectional angles of attack, blade sectional lift distributions, and inflow characteristics.

Blade structural characteristics

A good starting point for validation of the CAMRAD II model is to correlate the rotor blade dynamic characteristics with measurements. An accurate prediction of the blade dynamic characteristics is critical for rotorcraft designers to evaluate the susceptibility of the rotor blade to aeroelastic instability and to estimate vibratory loads. A previous study [11] compared the measured rotating natural frequencies and damping ratios to the CAMRAD II model with good agreement. However, no validation was done for the mode shapes. The current study extends the comparison to mode shapes of a rotor blade along the quarter-chord axis by using an algorithm called Complexity Pursuit (CP).

The Complexity Pursuit algorithm is classified under the family of Blind Source Separation (BSS) algorithms. The experimental modal parameter identification process in this study begins with application of the CP algorithm to the measured blade deformation. Note that this deformation consists of a steady component due to the mean aerodynamic loading in hover, as well as an unsteady component due to random excitation on the rotor blade. The source of this random excitation could be turbulence, rotor support vibration, or a number of other environmental effects. It is assumed that this excitation is random in time, i.e., it can be represented by a zero-mean Gaussian distribution.

Signals measured in any physical system are a mixture of statistically independent "source" signals [19]. In general, BSS is a methodology that allows identification and separation of these sources without any apriori input information. The usefulness of BSS techniques has been demonstrated for a diverse variety of data analyses. The application to structural analysis was introduced by Roan et al. [20] for damage detection and condition health monitoring of structures. Kerschen et al. [21] performed structural modal analysis using a BSS algorithm with numerical validation. The mathematical development of the algorithm is as follows:

Consider the differential equation of motion for a multi-degree-of-freedom structure

$$\mathbf{M}\ddot{\mathbf{x}}(t)+\mathbf{C}\dot{\mathbf{x}}(t)+\mathbf{K}\mathbf{x}(t)=\mathbf{F}(t) \tag{1}$$

where $\mathbf{M}$, $\mathbf{C}$, and $\mathbf{K}$ are the mass, damping, and stiffness matrices respectively, $\mathbf{F}(t)$ is the force vector, and $\ddot{\mathbf{x}}(\mathbf{t})$, $\dot{\mathbf{x}}(t)$, and $\mathbf{x}(t)$ are the acceleration, velocity, and displacement vectors at time t. Then modal transformation can be expressed as

$$\mathbf{x}(t)=\mathbf{\Phi}\boldsymbol{\eta}(t) \tag{2}$$

where $\mathbf{\Phi}$ and $\boldsymbol{\eta}$ are the modal matrix and modal coordinates of the system, respectively. Note that the modes of a system form, by definition, a linearly independent set of basis vectors [22]. Now let us introduce the general concept of BSS in mathematical form as

$$\mathbf{y}(t)=\mathbf{x}(t)+\mathbf{n}(t)=\mathbf{A}\,\mathbf{s}(t)+\mathbf{n}(t) \tag{3}$$

where $\mathbf{y}$ is the measured displacement vector at time t, $\mathbf{n}$ is a noise vector, $\mathbf{s}$ is the source vector, and $\mathbf{A}$, often called mixing matrix, is the transfer function matrix between sensors and sources. As shown in Equation 3, the usage of BSS within the context of operational modal analysis is to estimate the mixing matrix $\mathbf{A}$ and the source vector $\mathbf{s}$ from the measured output responses, and interpret them as the modal matrix $\mathbf{\Phi}$ and modal coordinates $\boldsymbol{\eta}$ of the structural system.

This idea can significantly simplify the multi-degree-of-freedom modal parameter identification due to the fact that each separated source ideally represents the equivalent single-degree-of-freedom response, whose frequency and damping ratio are associated with each structural mode. Mode shapes are represented by the mixing matrix $\mathbf{A}$. It should be noted that the dimension of the estimated modal matrix is $N \times N$, where N is the number of measurement points, meaning that BSS separates the measured data into N different source signals. A number of techniques falling under the broad spectrum of BSS can be found in the literature. These techniques share the fact that apriori information about the sources or the input forcing is not required.

Complexity Pursuit (CP) is a specific type of BSS technique. The formulation of CP was first introduced by Stone [23] in the field of neural computation, and applied to structural modal parameter extraction by Yang and Nagarajaiah [24]. The CP algorithm separates source signals by using a measure of signal complexity called temporal predictability. The temporal predictability of a signal is a measure describing how well one can predict the value of a signal at the next time step, knowing only the values of the signal at the previous time steps. The temporal predictability $G(y_i)$ of a signal is given by

$$G(y_i)=\log\frac{\sum_{j=1}^{N}(y_i(t_j)-\bar{y}_i(t_j))^2}{\sum_{j=1}^{N}(y_i(t_j)-\hat{y}_i(t_j))^2} \tag{4}$$

with y_i being a signal at i th measurement channel with N entries and $\bar{y}_i$ and $\hat{y}_i$ being the long-term and short-term predictors respectively, which are predefined parameters. Stone's algorithm is based on the theorem that the temporal predictability of a mixture of source signals is lower than that of each contained source signal, i.e., each source signal, or mode, is less complex than the measured signal, or superposition of modes. The algorithm tries to find the

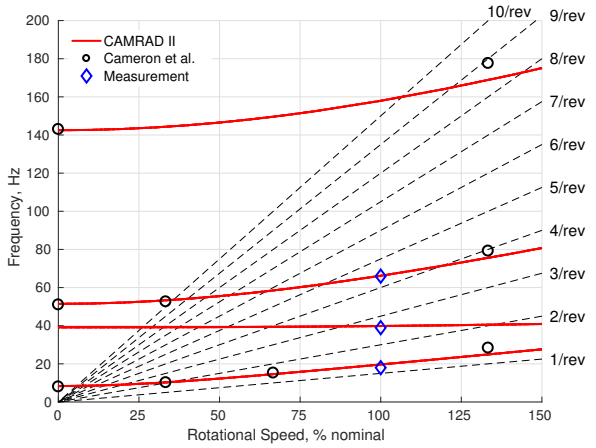

Fig. 6: Fanplot with numerical and measured natural frequencies (100% = 900 RPM).

mixing matrix $\mathbf{A}$ of the system, so that the temporal predictability of each resulting source is as high as possible.

This optimization approach eventually leads to solving an eigenvalue problem. The resulting matrix $\mathbf{W}$ of eigenvectors corresponds to the transpose of the mixing matrix $\mathbf{A}$. The source signals are then found by solving the inverse problem

$$\mathbf{s} = \mathbf{A}^{-1}\mathbf{y} = [\mathbf{W}^T]^{-1}\mathbf{y}. \tag{5}$$

More details on this method can be found in the literature [23].

The CP algorithm was used to extract the rotating natural frequencies of the blade from deformation measurements of the 1×1-bladed CCR rotor operating at low collective pitch. The fanplot in Fig. 6 shows the natural frequencies derived from the measured deformation using the CP (at 900 RPM), along with numerical predictions. Note that the natural frequencies at 300, 600, and 1200 RPM were obtained in previous experiments by Cameron et al. [11], who used a different modal identification algorithm on the same experimental setup. Overall, the correlation of the natural frequencies between the experimental and numerical results was very good over different rotor rotational speeds.

Figure 7 shows the first and second flap as well as the first lag rotating mode shapes compared to predicted results from CAMRAD II. For the three mode shapes, there was excellent agreement between the numerically predicted characteristics and the results obtained by the CP algorithm. This demonstrates that the operational modal analysis with the DIC deformation measurement is a powerful tool to identify the mode shapes of a rotating rotor blade, in addition to deriving modal frequencies.

However, it is worth mentioning here that the modes higher than the second flap mode were not well identified. This could be caused by the limitation of measuring the smaller deformations at higher frequencies by means of DIC. Another possible reason is that the measured data in the single-bladed coaxial rotor used in this study contained

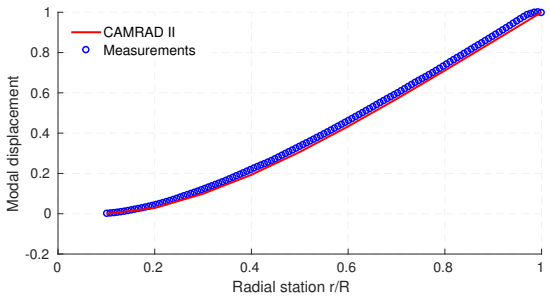

(a) 1st flap mode (18 Hz).

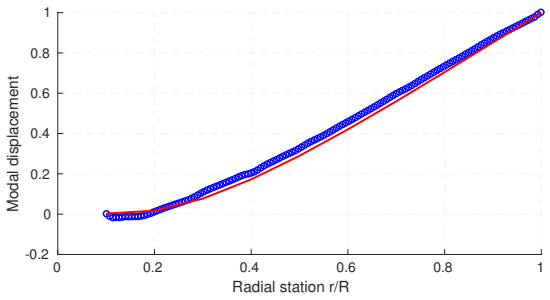

(b) 1st lag mode (39 Hz).

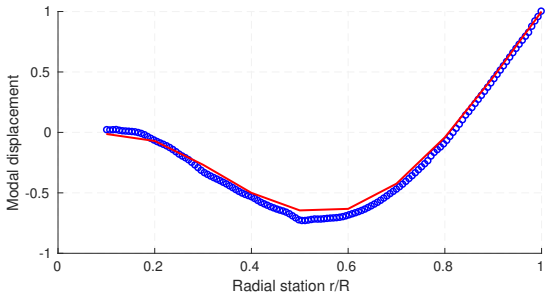

(c) 2nd flap mode (66 Hz).

Fig. 7: Rotating mode shapes of the first three modes at nominal rotational speed (900 RPM).

strong one-per-revolution vibrations, resulting in harmonic excitations to measured responses at integer multiples of the rotational frequency (15 Hz). The harmonic components could violate the assumption of the operational modal analysis, i.e., that the excitation to the structure is random and represented by a zero-mean Gaussian distribution. To highlight the harmonic components, Fig. 8 shows the Fourier transform of the source signals corresponding to the first flap mode shape. Recalling that each separated source ideally contains one single frequency, the frequency spectrum of the source corresponding to a physical mode should ideally show a single peak at the modal frequency. However, it is quite obvious that there were large peaks associated with the harmonics of one-per-revolution frequency in the spectrum.

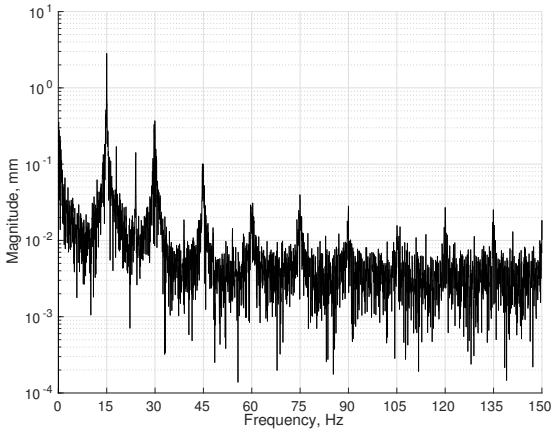

Fig. 8: Frequency spectrum of the source signal for the first flap bending mode.

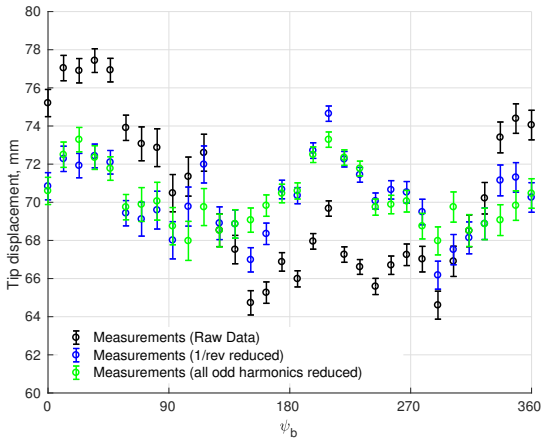

Fig. 9: Effect of harmonics reduction on the measured lower rotor blade tip path.

Blade deformations

Blade deformations from transient aerodynamic loading due to blade passage were analyzed using a combined experimental and numerical approach. Furthermore, the validation effort of the CAMRAD II blade structural model was hereby continued and progressively verified by comparing the obtained blade flapwise deformations with the measurements of the 1×1-bladed coaxial rotor system. Note that theoretically, a balanced 1×1-bladed CCR rotor with identical blades can generate only harmonics of 2/rev in blade deformation and loads. However, due to a number of non-ideal factors in the experimental setup, for example, blade-to-blade dissimilarities, the measured data showed large 1/rev and other odd harmonics; see Fig. 8. For a better comparison with the numerical model and to focus on the effect of interactional aerodynamics, these spurious 1/rev and odd harmonics must be filtered out from the measurements.

Figure 9 quantifies the effect of filtering out the odd harmonics from the measured out-of-plane deflections of the lower rotor blade at $C_T/\sigma = 0.09$; deformations are at quarter-chord. This plot shows the unfiltered data (shown in black) over one rotor revolution with measurement uncertainty at each of the 32 measurement points. It also shows data with the first rotor harmonic component reduced (shown in blue) and the results for the data that were with all of the odd harmonics reduced (shown in green). The 1/rev harmonics reduction already revealed significant 2/rev characteristics, and there was minimal effect from reducing the higher odd harmonics. Therefore, the measured data with 1/rev content reduced are used in all subsequent discussions. Predicted CAMRAD II results correlated satisfactorily with these measurements in both magnitude and phase; see Fig. 10. Both experiments and numerical results revealed dominating 2/rev characteristics that correspond to the effects of the blade passage.

With the blade crossings located at $\psi_b = 0^\circ$ and 180°, the lower rotor blade responded to the transient blade loads resulting in the clearly identifiable 2/rev characteristics. Maximum peaks of blade deflections were located at about $\psi_b = 30^\circ$ and 210°. For the lower rotor disk loading of $C_T/\sigma = 0.09$, oscillations around the mean deflection of 69.6 mm occurred with maxima at 74.6 mm and minima at 66.4 mm. The 2/rev half-peak-to-peak magnitudes of 4.1 mm corresponded to 5.9% of the mean deflection. Note that this percentage will depend on varying disk loading and inter-rotor spacing.

Figure 10 furthermore shows the numerically predicted blade tip path for the upper coaxial rotor. Compared to the lower rotor, the upper rotor exhibited a larger mean deformation because of the greater thrust produced by the upper rotor (in this torque-balanced coaxial rotor configuration). This observation was also discussed in a previous study [11] using experiments, and in more recent work using both analysis and experiments [1]. In terms of interactional effects, these studies also showed that the effect of the upper rotor on the lower rotor was more significant than the effect of the lower rotor on the upper rotor.

This behavior was also evident in the similar but less pronounced 2/rev magnitude of the upper rotor blade tip path compared to that of the lower rotor, although the upper rotor blade had a larger mean deflection; see Fig. 10. Furthermore, respective phases of maximum and minimum peaks were shifted by about 15° compared to those of the lower rotor. Higher harmonic effects from, e.g., the 4/rev, were seen at least in the numerical analysis (measured fluctuations obscured these characteristics in the current experiments), and they will be investigated further by modeling and testing.

Figure 11 shows a comparison between measured and predicted blade deformation of the lower rotor blade as a function of radial station. The two curves correspond to the maximum and minimum peak locations that were previously determined from Fig. 10. Numerical results correlated well with the test data while slightly over-predicting the minimum blade deformation. Because of the radial distribution of the aerodynamically induced blade loads and

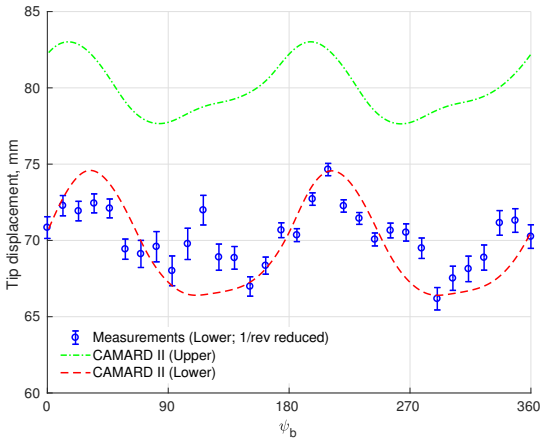

Fig. 10: Upper (numerics only) and lower coaxial rotor blade tip path.

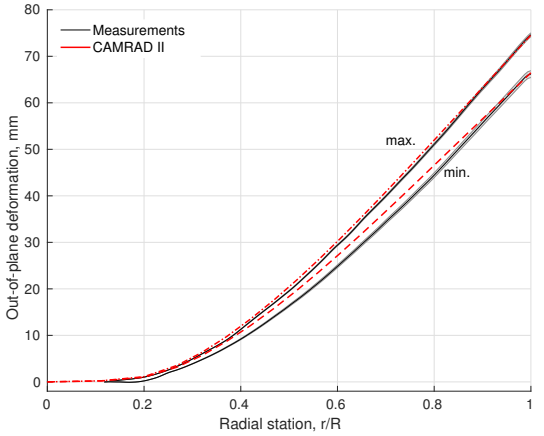

Fig. 11: Maximum and minimum lower rotor blade out-of-plane deformation as a function of radial station.

the increased flap bending moment inboard, the curvature of the out-of-plane blade deformation increased from outboard to inboard regions. Note that the blades had homogeneous structural properties [13] along the aerodynamically effective blade span.

The measured out-of-plane lower rotor blade deformation over the entire rotor disk is shown in Fig. 12a and compared to numerical predictions in Fig. 12b. These contour plots give another perspective on the data shown in Figs. 10 and 11, as they show all the data in the deflection matrices over all radial and azimuthal positions. Again, the maximum deflections occurred at about $\psi_b = 30°$ and 210°. Overall, the DIC measurement technique proved its capability to measure the rotor blade flapping motion over the entire rotor disk. It provides useful measurements for the validation of numerical analysis models and helps with the investigations on coaxial rotor transient blade loadings and deformations.

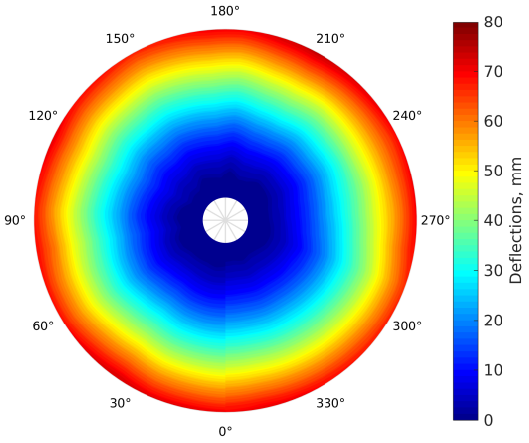

(a) Measurement.

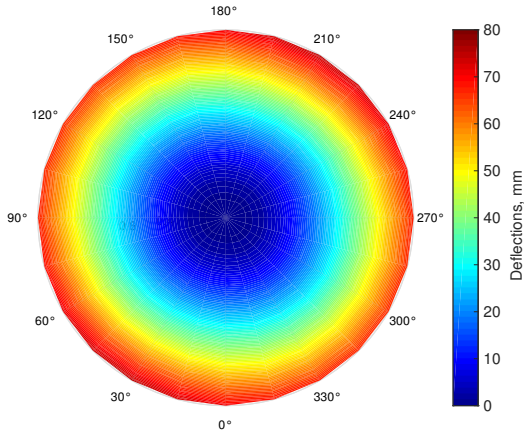

(b) CAMRAD II.

Fig. 12: Polar plots of lower rotor blade out-of-plane deformation.

Rotor hub and pitch link loads

The mean and the vibratory loads on the rotor hubs and pitch links are examined in this section. This is again performed by a combined experimental and numerical approach, with extended numerical studies to further the understanding of the aerodynamic forcing of the transient blade loads.

The need for processing the measurement to reduce odd rotor harmonics in the measurements was discussed previously (see Section). Figure 13 shows the unprocessed measurements of lower rotor axial hub load (rotor thrust) over one rotor revolution with measurement uncertainty represented by a shaded region. Also shown is filtered data consisting of only (a) 2/rev harmonic, (b) 2/rev and 4/rev harmonics, and (c) 2/rev, 4/rev and 6/rev harmonics. To highlight the contribution of each harmonic component to the rotor thrust, Fig. 14 shows the individual harmonic magnitudes up to the 9/rev components from unprocessed measurements and CAMRAD II.

The large 1/rev component as well as non-negligible

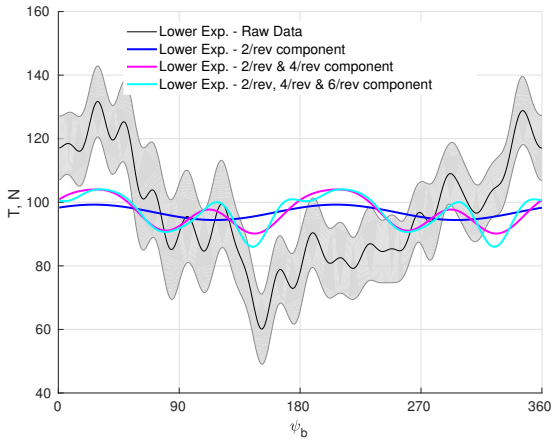

Fig. 13: Unprocessed and filtered measurements of lower rotor thrust T^L.

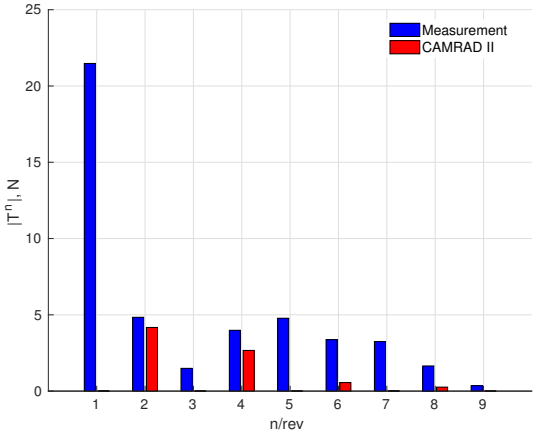

Fig. 14: Harmonics of lower rotor thrust T^L, measurements and CAMRAD II.

higher harmonics were apparent in the experimental data. Note that the numerical predictions show only even harmonics because inertial and aerodynamic contributions in a 1×1-bladed CCR rotor configuration can only contain harmonics that are multiples of 2/rev. From Fig. 14, the magnitudes of the 2/rev and 4/rev harmonics are seen to correlate well between CAMRAD II and the experiments. It can also be seen that harmonics higher than 6/rev do not have a significant effect on the hub loads and pitch link loads. Therefore, in subsequent discussions, only the 2/rev, 4/rev, and 6/rev components of the measurements are retained.

Figure 15 shows the measured and predicted lower rotor thrust as a function of rotor azimuth angle. Recall that the experimental data were reconstructed using only the 2/rev, 4/rev, and 6/rev harmonics; see also Fig. 13. Although general trends correlated between the numerical model and the experiments (with the CAMRAD II results always being within the error bounds of the measurements) excursions in the test data were seen that were not predicted by the numerical model. As previously stated, the even harmonics correlated well, and in particular the important 2/rev and 4/rev harmonics; see Fig. 14. The thrust increased when the

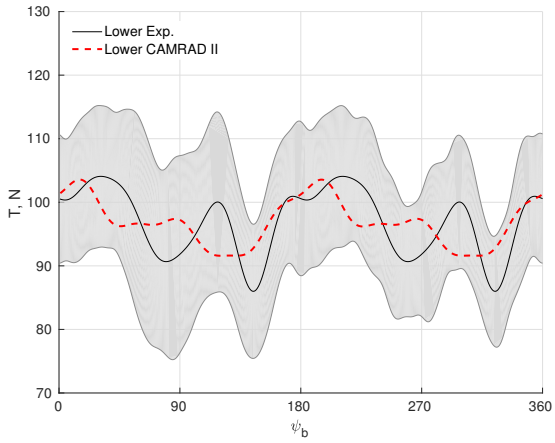

Fig. 15: Lower coaxial rotor thrust T^L, with filtered experimental data and CAMRAD II predictions.

upper and lower rotor blades approached each other. This was caused by interactional upwash induced by the upper on the lower rotor. The peaks in the thrust distribution were observed between about $\psi_b = 15^\circ$ (CAMRAD II) and $\psi_b = 30^\circ$ (measurements) for the first blade crossing, and between about $\psi_b = 195^\circ$ (CAMRAD II) and $\psi_b = 210^\circ$ (measurements) for the second blade crossing.

Note that the blade crossed each other at $\psi_b = 0^\circ$ and $\psi_b = 180^\circ$ in the model and in the experiments. Hence, when neglecting the error bounds from the test data, slight phase shifts of peak loadings were observed, whereas in previous studies (although at slightly different operating conditions) they matched very well in both magnitude and phasing concerning the rotor thrust [11]. The measurements also showed additional peaks at about $\psi_b = 120^\circ$ and $\psi_b = 300^\circ$ that were not captured in the predictions, and these are currently under investigation. However, both the measurement and the prediction captured the 2/rev vibratory thrust caused by the periodic blade crossings, and the predicted thrust was within the measurement uncertainty.

Figures 16 to 18 show the harmonics reduction of the pitch link loads (see Fig. 16), the amplitudes of each harmonic component (see Fig. 17) of both measurements and CAMRAD II, and filtered measurements of pitch link loads as a function of azimuthal location and compared to numerical results. Similar to the case of the rotor thrust measurements (see Fig. 13), a large 1/rev signal dominated the pitch link load measurements. Therefore, the same method of filtering, i.e., retaining only the 2/rev, 4/rev and 6/rev harmonics, was applied to the measured pitch link loads.

Comparing the numerical results to the filtered measurements, the dominating 2/rev harmonics were well predicted, but they showed a phase shift of about $\psi_b = 60^\circ$. Figure 17 also shows that the 2/rev magnitudes were more pronounced in the measurements compared to the results from the analytical model. The 4/rev characteristics, as a multiple of the 2/rev, were also clearly visible in measurement and analysis.

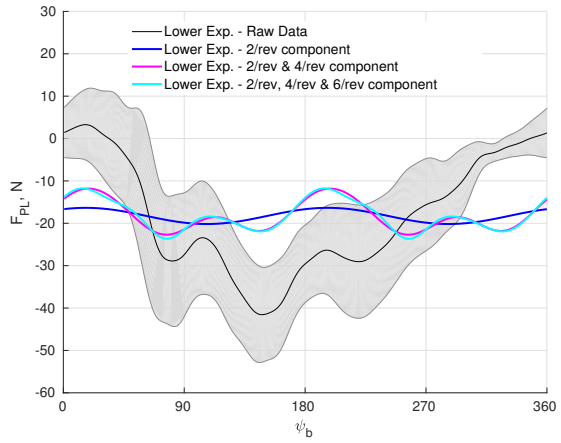

Fig. 16: Unprocessed and filtered measurements of pitch link loads F_{PL}^{L}.

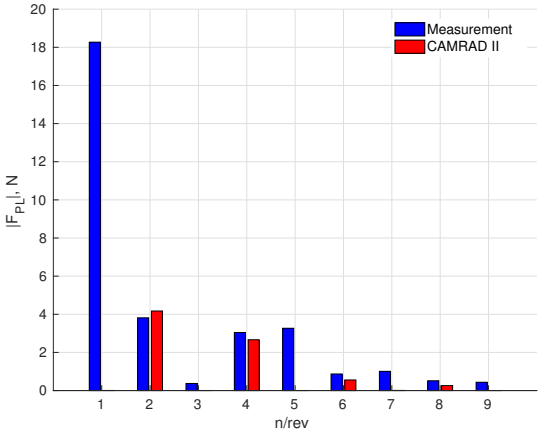

Fig. 17: Harmonics of the lower rotor pitch link loads F_{PL}^{L}, measurements and CAMRAD II.

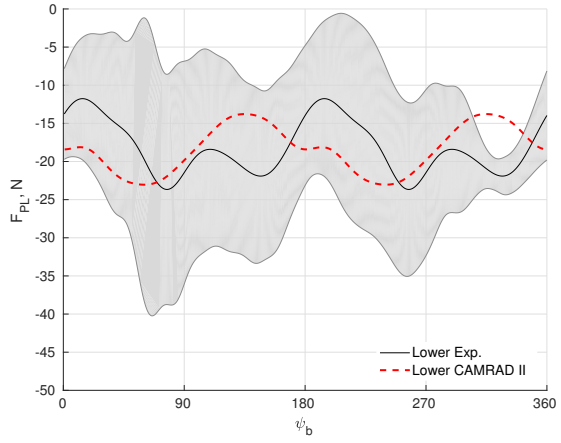

Fig. 18: Lower rotor pitch link loads F_{PL}^{L}, with filtered experimental data and CAMRAD II predictions.

Understanding of transient blade loads

With the CAMRAD II model satisfactorily validated by measurements, the CAMRAD II analysis can now provide additional information that may yield insights into further understanding the fundamental phenomena and physics responsible for interactional loads in a CCR rotor system. Figure 19 shows contour plots of sectional angle of attack for both the upper and the lower rotor disk. In general, in hover the mean aerodynamic angles of attack at the upper rotor are larger compared to the lower rotor, because of the interactional aerodynamics inducing smaller angles of attack on the lower rotor, and so the lower rotor also produces less mean thrust than the upper rotor in a torque-balanced CCR rotor system. Maximum angles of attack along the blade span were detected at approximately 75%R.

Figure 19 also indicates that the angle of attack was strongly influenced by the upper and lower rotor blade passage. This 2/rev periodic event was seen on both the upper and the lower rotor. Aerodynamic angles of attack increased steadily up to the azimuth of blade crossing. They then reached a maximum just before the crossings (about $\psi_b = 15^\circ$ before) because of induced inflow velocities and induced angles of attack from the blade bound circulation of the other rotor blade. Because of the change in sign that the other rotor blade sees from the blade bound vortex sweeping by, the angles of attack dropped to a minimum right after blade passage (i.e., about $\psi_b = 15^\circ$ after). This phasing was consistent with the trends observed in the unsteady hub loads as well as in the rotor blade deformations, and they were similar for upper and lower rotors of the CCR rotor system.

These varying induced velocities on the other rotor are shown by the interactional inflow velocity distribution over the rotor disk for the upper and lower rotor; see Fig. 20. The interactional inflow velocity was defined as the inflow components that were induced solely by one rotor on the other, neglecting any self-induced effects. It emphasizes the unsteady aerodynamic interference between the rotors. The induced inflow velocities from rotor–rotor interactions of the upper and lower rotor gradually increased as the blades approached each other. These characteristics correlated with the previous observations for the angles of attack, and they emphasize the importance of the interactional aerodynamics on the transient loads. As expected, the greatest magnitudes of interactional inflow velocities occurred at about $\psi_b = 15^\circ$ after each blade crossing, where the aerodynamic angles of attack were at a minimum.

The inflow velocity variation over a blade crossing was caused by the aforementioned wake interaction, i.e., by an upwash and downwash induced by one rotor on the other that increased or reduced the inflow of the blade, resulting in the reduction of angles of attack when the interactional inflow was greatest. Figure 20 clearly shows greater interactional effects from the upper rotor on the lower rotor; to a lesser extent, the lower rotor induced an inflow change at the upper rotor. The high inflow velocity region over ap-

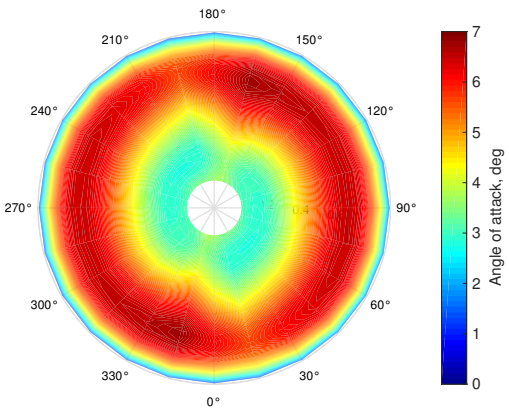

(a) Upper rotor.

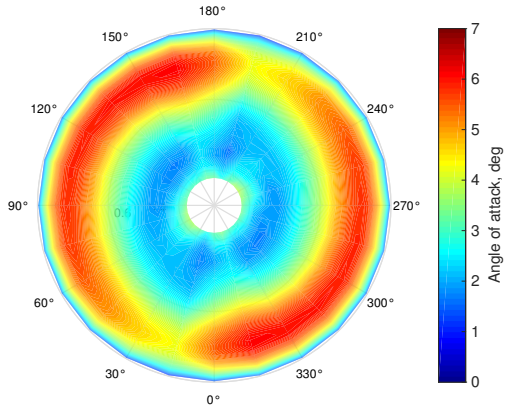

(b) Lower rotor.

Fig. 19: Aerodynamic angles of attack.

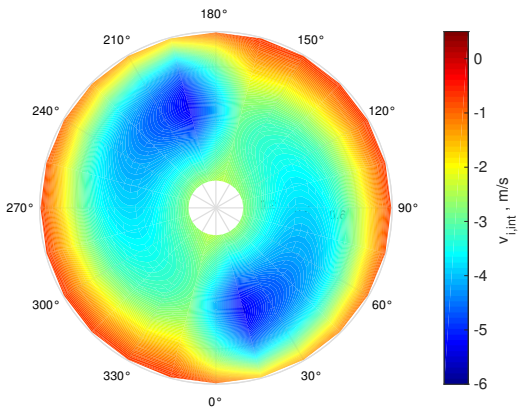

(a) Upper rotor.

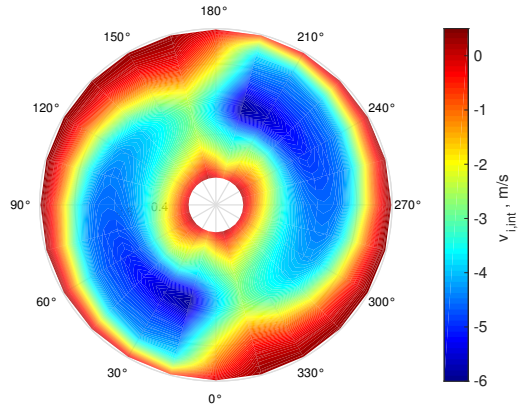

(b) Lower rotor.

Fig. 20: Interactional inflow velocities, v_{int}.

proximately $15° - 30°$ degrees of rotor azimuth was consistent with the rotor blade flap bending response, whose peak was observed in almost the same azimuthal region; see Fig. 10. Overall, the numerical analysis was able to capture the complex rotor blade–inflow coupling dynamics that are the primary physical reason for transient blade loads on such a closely-spaced coaxial rotor system.

Sectional loads on the rotor blades are of interest because of the radially varying influence from the aerodynamically interacting rotor blades on the lift distribution over the rotor disk. The integrated rotor thrust over the blade azimuth was previously shown in Fig. 15; this thrust includes both aerodynamic and inertial effects. Figure 21 shows the predicted blade sectional loads distribution (normal to the rotor plane), F_Z, over the entire upper and lower rotor disks. These sectional loads were obtained from a force balance and thus include both aerodynamic and inertial loads. Similar to the angle of attack distribution (see Fig. 19), the 2/rev characteristics are clearly observed, which is an inherent vibratory component of the 1×1-bladed CCR rotor configuration. There was an increase and decrease of F_Z, particularly in the outboard regions at about 80% to 90% of the rotor radius. The variation of F_Z in the azimuthal regions near the blade crossings (see, e.g., from $\psi_b = 345°$ to $15°$) corresponded to the region of strongly varying induced angles of attack; see Fig. 19.

5. SUMMARY AND CONCLUSIONS

This paper described a combined experimental–numerical approach to examine the complicated aeromechanics of a rigid, closely-spaced, coaxial counter-rotating (CCR) rotor system. Transient rotor blade response due to periodic blade passage was investigated. Hub loads, pitch link loads, rotor blade deformations, as well as rotating blade natural frequencies and mode shapes were measured for a reduced-scale, 2m-diameter, 1×1-bladed CCR rotor system in hover and correlated to numerical predictions of a CAMRAD II model.

Blade deformations measured over the entire rotor disk using digital image correlation (DIC) were used to extract rotating-frame natural frequencies and mode shapes using the Complexity Pursuit algorithm. These dynamic characteristics showed good agreement with numerical CAMRAD II predictions. The time history of the out-of-plane blade deformations and the rotor loads exhibited significant contributions from 1/rev and other odd harmonics. This was attributed to non-ideal effects in the experimental setup

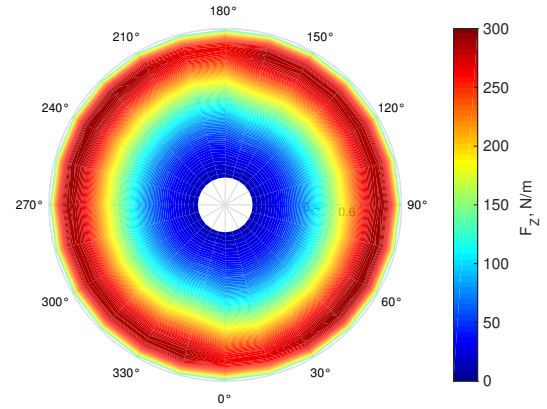

(a) Upper rotor.

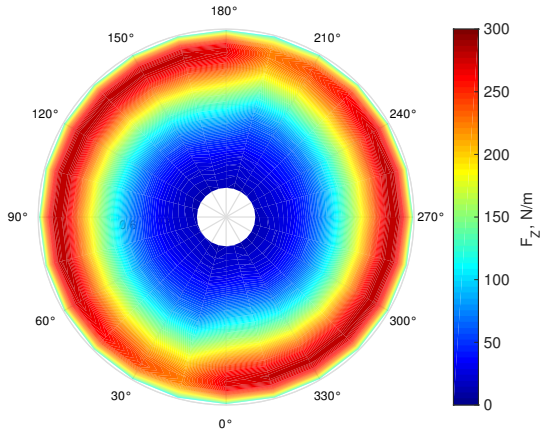

(b) Lower rotor.

Fig. 21: Distribution of sectional load, F_Z, normal to the rotor plane.

such as those induced by blade dissimilarities. Therefore, the measurements were filtered to reduce the 1/rev and odd harmonic content.

The magnitude of 2/rev blade tip displacement was found to be 6% of the mean tip displacement. Although the upper rotor blade tip had a larger mean displacement than the lower rotor blade tip due to the larger share of thrust carried by the upper rotor, the magnitude of 2/rev transient blade tip displacement was larger in the lower rotor than in the upper rotor. This indicates that for transient interactional aerodynamic effects, the upper rotor has a larger influence on the lower rotor than vice versa.

It was observed that even harmonics above 6/rev did not contribute significantly to the measured loads. Hence, only the 2/rev, 4/rev, and 6/rev harmonics were retained for comparison to CAMRAD II predictions. The magnitudes and the phasing of out-of-plane bending deformations were well predicted by the numerical analysis for a set rotor thrust. The predicted hub loads and pitch link loads also showed satisfactory agreement with the measurements, and although some discrepancy in the phase was found, the predictions generally remained within the measurement uncertainty.

The numerical model was used to further explore the aerodynamic forcing, i.e., the source of the investigated transient loads from blade passage, by means of angle of attack distribution and interactional inflow over the upper and lower rotor disks. It was found that the angle of attack reached a maximum at 15° azimuth before the blade crossings, and decreased to a minimum at 15° azimuth after the blade crossings. The interactional inflow on the lower rotor, i.e., the inflow component on the lower rotor that was caused by the upper rotor, reached a maximum at 15° after the blade crossing, i.e., where the local angles of attack were at a minimum. Furthermore, the radial distribution of the wake interaction was analyzed by the sectional loads distribution normal to the rotor plane, showing the aerodynamically predominant 2/rev characteristics from blade passage, particularly in the outboard regions at about 80% to 90% of the rotor radius.

Future work includes improvements to the test setup to minimize the 1/rev and odd harmonic content of the measured blade deformations and loads. The measured blade deformation can be used to calculate the inertial loads. These, in conjunction with measured hub loads, can be used to extract the transient aerodynamic loads due to blade passage that can be used for further validation of the computational model. Accurate prediction of the transient loads will provide a foundation to develop methods to mitigate vibration in CCR rotor systems.

ACKNOWLEDGEMENTS

This research was funded in part by the U.S. Army, Navy, and NASA Vertical Lift Research Center of Excellence (VLRCOE) program with Dr. Mahendra Bhagwat as the technical monitor.

REFERENCES

[1] Feil, R., Rauleder, J., Cameron, C. G., and Sirohi, J., "Aeromechanics Analysis of a High-Advance-Ratio Lift-Offset Coaxial Rotor System," *Journal of Aircraft*, 2018.

[2] Walsh, D., Weiner, S., Arifian, K., Lawrence, T., Wilson, M., Millott, T., and Blackwell, R., "High Airspeed Testing of the Sikorsky X2 Technology^{TM} Demonstrator," Proceedings of the American Helicopter Society 67th Annual Forum, Virginia Beach, VA, May 3–5, 2011.

[3] Cameron, C. and Sirohi, J., "Performance and Loads of a Model Coaxial Rotor Part I: Wind Tunnel Testing," Proceedings of the American Helicopter Society 72th Annual Forum, West Palm Beach, Florida, 2016.

[4] Blackwell, R. and Millott, T., "Dynamics Design Characteristics of the Sikorsky X2 Technology Demonstrator^{TM} Aircraft," Proceedings of the American Helicopter Society 64th Annual Forum, Montréal, Québec, April 29–May 4, 2008.

[5] Cameron, C., Karpatne, A., and Sirohi, J., "Performance of a Mach-Scale Coaxial Counter-Rotating Rotor in Hover," *Journal of Aircraft*, Vol. 53, No. 3, May 2016, pp. 746–755.

[6] Feil, R., Rauleder, J., and Hajek, M., "Vibratory Load Predictions of a High-Advance-Ratio Coaxial Rotor System Validated by Wind Tunnel Tests," Proceedings of the 43rd European Rotorcraft Forum, Milan, Italy, September 12–14, 2017.

[7] Kufeld, R., Balough, D., Cross, J., Studebaker, K., Jennison, C., and Bousman, W., "Flight Testing of the UH-60A Airloads Aircraft," Proceedings of the American Helicopter Society 50th Annual Forum, Washington D.C., May 11–13, 1994.

[8] van der Wall, B. G., Burley, C. L., Yu, Y., Richard, H., Pengel, K., and Beaumier, P., "The HART II test – measurement of helicopter rotor wakes," *Aerospace Science and Technology*, Vol. 8, No. 4, 2004, pp. 273 – 284.

[9] Uehara, D., Cameron, C., and Sirohi, J., "Deformation Measurement and Modal Identification of an Extremely Flexible Rotor Blade," Proceedings of the 6th Asian/Australian Rotorcraft Forum/ Heli Japan, Kanazawa, Japan, November 7–9, 2017.

[10] Uehara, D., Eitner, M., and Sirohi, J., "Automated Operational Modal Identification of a Rotor Blade," Proceedings of the American Helicopter Society 74th Annual Forum, Phoenix, AZ, May, 14–17, 2018.

[11] Cameron, C. G., Feil, R., Sirohi, J., and Rauleder, J., "Measurement of Transient Loads and Blade Deformation in a Coaxial Counter-Rotating Rotor," Proceedings of the American Helicopter Society 73rd Annual Forum, Fort Worth, TX, USA, May 9–11, 2017.

[12] Johnson, W., "Technology Drivers in the Development of CAMRAD II," American Helicopter Society Aeromechanics Specialists Conference, San Francisco, CA, USA, January 19–21, 1994.

[13] Feil, R., Rauleder, J., and Hajek, M., "Aeromechanics Analysis of a Coaxial Rotor System in Hover and High-Advance-Ratio Forward Flight," 34th AIAA Applied Aerodynamics Conference, AIAA Aviation, Washington, DC, USA, June 13–17, 2016.

[14] Schmaus, J. and Chopra, I., "Validation of Predicted Vibratory Loads of a Coaxial Rotor at High Advance Ratios with Wind Tunnel Test Data," Proceedings of the 42nd European Rotorcraft Forum, Lille, France, September 6–8, 2016.

[15] Bagai, A. and Leishman, J. G., "Rotor Free-Wake Modeling Using a Pseudo-Implicit Technique Including Comparisons with Experimental Data," *Journal of the American Helicopter Society*, Vol. 40, No. 3, 1995, pp. 29–41.

[16] Leishman, J. G., Bhagwat, M. J., and Bagai, A., "Free-Vortex Filament Methods for the Analysis of Helicopter Rotor Wakes," *Journal of Aircraft*, Vol. 39, No. 5, 2002, pp. 759–775.

[17] Lim, J. W., Yu, Y. H., and Johnson, W., "Calculation of Rotor Blade-Vortex Interaction Airloads Using a Multiple-Trailer Free-Wake Model," *Journal of Aircraft*, Vol. 40, No. 6, 2003, pp. 1123–1130.

[18] Johnson, W., *Rotorcraft Aeromechanics*, Cambridge Aerospace Series, Cambridge University Press, 2013.

[19] Comon, P. and Jutten, C., *Handbook of Blind Source Separation: Independent Component Analysis and Applications*, Academic Press, 2010.

[20] Roan, M. J., Erling, J. G., and Sibul, L. H., "A New Non-linear, Adaptive, Blind Source Separation Approach to Gear Tooth Failure Detection and Analysis," *Mechanical Systems and Signal Processing*, Vol. 16, No. 5, 2002, pp. 719–740.

[21] Kerschen, G., Poncelet, F., and Golinval, J. C., "Physical Interpretation of Independent Component Analysis in Structural Dynamics," *Mechanical Systems and Signal Processing*, Vol. 21, No. 4, 2007, pp. 1561–1575.

[22] Meirovitch, L., *Fundamentals of Vibrations*, McGraw-Hill Book, New York, NY, 2000, Chapter 7.

[23] Stone, J., "Blind Source Separation Using Temporal Predictability," *Neural Computation*, Vol. 13, 2001, pp. 1559–1574.

[24] Yang, Y. and Nagarajaiah, S., "Blind Modal Identification of Output-only Structures in Time-domain Based on Complexity Pursuit," *Earthquake Engineering Structural Dynamics*, Vol. 42, 2013, pp. 1885–1905.